Nanometer-thick Mn:NiO and Co:NiO films for high performance nonenzymatic biosensors

Nanometer-Thick Mn:NiO and Co:NiO Films for High Performance Non-enzymatic Biosensors

Yusuf Tutel[1,a], Serkan Koylan[1,a], Sensu Tunca[1,2] and Husnu Emrah Unalan[1,3,*]

[1] Department of Metallurgical and Materials Engineering, Middle East Technical University (METU), 06800 Ankara, Turkey.

[2]Antwerp Electrochemistry and Analytical Science Lab (A-Sense), Department of Bioscience Engineering, University of Antwerp, B-2020, Antwerpen, Belgium.

[3]Energy Storage Materials and Devices Research Center (ENDAM), Middle East Technical University (METU), 06800 Ankara, Turkey.

Abstract

People with diabetes require regular blood sugar level monitoring, using commercial enzyme-based biosensors. There is a considerable need to develop biosensors with non-enzymatic electrodes to eliminate the drawbacks of enzymes. Nanostructured nickel oxide (NiO) thin films are highly promising materials for the development of non-enzymatic glucose and hydrogen peroxide (H_2O_2) biosensors. Although the biosensor performance can be easily attained with non-enzymatic electrodes, their commercialization still requires development of cost effective and mass-production methods. In this work, we demonstrate the use of ultrasonic spray deposited, nanometer-thick, bare NiO and manganese and cobalt doped NiO (M:NiO (M: Mn and Co)) thin films on indium tin oxide (ITO) coated glass substrates for glucose sensing. Sensor characterization followed detailed materials characterisation. Co:NiO nanometer-thick film electrodes showed better glucose sensor performance than those of bare NiO and Mn:NiO electrodes. High sensitivity of 1.67 $\mu A/\mu M \cdot cm^2$, a low detection limit of 231 nM, and a fast response time of 5.4 s within the linear range of 16-308 μM was obtained from Co:NiO thin-film electrodes. Amperometric measurements showed significant electrode reproducibility and stability. Co:NiO thin film electrode was also used to demonstrate actual clinical glucose measurements using human blood serum as a glucose source. Moreover, all fabricated nanometer-thick film electrodes were also utilized as H_2O_2 sensors. This work provides a novel approach for monitoring the biosensor performance using doped NiO thin-film electrodes. Obtained results demonstrated the potential of ultrasonic spray deposition method for the mass-production of high-performance non-enzymatic thin film biosensors.

Keywords: doped nickel oxide, thin film electrodes, ultrasonic spray deposition, glucose sensor, hydrogen peroxide sensor

* *Corresponding Author: unalan@metu.edu.tr*

[a] *Authors equally contributed to this work.*

Introduction

The demand for biosensors has increased in the last decade due to the worldwide increase in the number of diabetes patients. Diabetes is a chronic disease that increases the level of glucose in the blood. If left undiagnosed and untreated, it can be very dangerous for health and ultimately result in death [1]. In this respect, accurate, reliable, periodic, and rapid detection of blood glucose levels is vital in diabetes. Conventional glucose biosensors require the use of enzymes; however, enzymatic glucose sensors have some limitations due to the intrinsic nature of enzymes, which can be easily affected by changes in pH, temperature, humidity, and the presence of other chemicals. In addition, they have high-cost and short-life due to the denaturation of enzymes [2–4]. Over the past years, non-enzymatic glucose sensors with fast response and high accuracy have been developed to overcome these limitations. Amperometric detection of various analytes with enzymeless methods became possible with the use of electrocatalytic materials. Similar to glucose, excess hydrogen peroxide (H_2O_2) may lead to serious health problems as diabetes, cardiovascular disorders, cancer, and concerning neurodegenerative diseases. An accurate, rapid, and reliable method to detect H_2O_2 is also of great importance [5]. Thus, it is necessary to develop non-enzymatic electrochemical sensors with high sensitivity, low cost, and high stability for both glucose and H_2O_2 detection.

Although studies showed that emergent materials could show enough sensitivity to glucose, there is an increasing interest in the fabrication of low-cost electrodes using transition metals such as copper [6,7], nickel [8] and transition metal oxides such as copper oxide [9], titanium oxide [10], nickel oxide [11,12,13], cobalt oxide [14] to construct non-enzymatic glucose biosensors. The properties of non-enzymatic sensors such as sensitivity, detection limit, response time, selectivity, and stability highly depend on the types and morphology of the materials [15–17]. The performance of the non-enzymatic sensors may be increased using different nanostructures like Pt-Pb alloy [18], Pt-Au alloy [19], Pt/Au surface[20], Ag-Pt core-shell NWs [21], Ni-Cu alloy [22], and Pt-Ag/Cu alloy [23]. Further, nanostructured materials typically show better analyte detection since they provide more surface area for reactions. Analyte selectivity is a crucial factor for biosensors because glucose coexists with lactic acid, urea, proteins, salts, etc. Traditionally, for the fabrication of biosensors, the prepared nanostructured materials are drop cast onto a conductive substrate with a binder. The electrical conductivity of the materials eventually decreases due to the loss of binder, introducing contact resistance [24]. Poor adhesion of the materials to the substrate is another problem. Therefore, these techniques are not suitable for the efficient and cost-effective production of amperometric sensors. Alternatively, solution-based deposition methods for functional thin films are cost-effective for the mass production of biosensor electrodes with high surface area and increased stability.

In particular, Ni and Ni-based nanomaterials exhibit high electrocatalytic activity for glucose in the alkaline medium due to the $Ni(OH)_2$/NiOOH redox couple, while glucose is directly oxidized to gluconolactone [25]. Similar to glucose detection, NiOOH / $Ni(OH)_2$ redox couples are demonstrated for H_2O_2 sensing when Ni-based nanomaterials are used as non-enzymatic active materials. There are numerous examples of Ni-based non-enzymatic glucose and H_2O_2 sensors constructed by modifying the substrate with nickel nanoparticles, nickel–carbon hybrids, Ni–CNT composite, Ni–graphene composites, $Ni(OH)_2$/C nanoparticles, $LaNiO_3$ nanooxide etc. [8,26–32,33,34]. It has also been demonstrated that the sensor characteristics may simply be tuned via doping the electrochemically active thin films. Ding et al. fabricated a novel amperometric non-enzymatic glucose sensor based on Au doped NiO nanobelts [35]. The hybrid

nanofiber modified electrode showed significantly lower initial potential, lower detection limit, higher sensitivity and broader linear range than the counterparts. This was due to increased electrocatalytic activity for the oxidation of glucose upon Au doping. Gao et al. synthesized tremella-like Mn-doped NiO nanomaterials (Mn:NiO) and utilized them for biomimetic glucose sensing in an alkaline medium [36]. Mn-NiO-based sensors demonstrated high sensitivity, fast response time, low limit of detection, and long-term stability for glucose detection compared to NiO-based sensors. On the other hand, only a few studies discussed the use of bare NiO nanometer-thick films for glucose [37–41] and H_2O_2 [37,42,43] biosensors. Although the biosensor performance of doped NiO nanomaterials has been explored, to the best of our knowledge, doping of NiO thin films to enhance their sensing properties in glucose/H_2O_2 biosensors has not been studied to date.

This work presents a direct deposition route to fabricate homogeneous and crack-free, bare and Mn and Co-doped NiO nanometer-thick films. The structural, morphological, chemical, optical and electrochemical properties of these thin films were comprehensively investigated. The fabricated thin-film electrodes were utilized as non-enzymatic amperometric glucose/H_2O_2 biosensors. The sensitivity, limit of detection, response time, and linear range of the electrodes were determined. A large-area (15 cm x 15 cm) thin film was used to demonstrate the functionality of the ultrasonic spray deposition (USD) method for electrode preparation, which allowed the obtainment of more than 250 electrodes in a single deposition. Our study demonstrated that the USD method is a versatile technique for the deposition of uniform, reproducible, high-quality bare and Mn and Co-doped NiO thin-film electrodes for high-performance biosensing applications.

2. Experimental Details

2.1.Materials

Microscopic glass slides were purchased from ISOLAB. The ITO/glass substrates were purchased from Delta Technologies LTD. (sheet resistance of 51-52 Ω/square). Ethanol (absolute, ≥ 99.8%), hydrogen peroxide (H_2O_2, ≥ 34.5-36.5%), L-Ascorbic acid (ACS reagent, ≥ 99.0%), D-(+)-glucose monohydrate (anhydrous, 97.5−102.0 %), DL-lactic acid (90%), oxalic acid dihydrate (ACS reagent, ≥ 99%), nickel nitrate hexahydrate ($Ni(NO_3)_2.6H_2O$), cobalt nitrate hexahydrate ($Co(NO_3)_2.6H_2O$) and manganese nitrate tetrahydrate ($Mn(NO_3)_2.4H_2O$) were purchased from Sigma-Aldrich. Sodium hydroxide (pellets pure, ≥ 99 %) was purchased from Merck. Deionized water (DI) (18.3 MΩ) was used in all steps. All chemicals were used without any purification.

2.2.Deposition of thin films

Microscopic glass slides and ITO/glass substrates were cut with different dimensions (i.e., 2 cm × 2 cm, 0.8 cm × 2.5 cm, and 15 cm x 15 cm) and cleaned consecutively with acetone, ethanol, and DI water for 20 min each using an ultrasonic bath. Then, all substrates were dried under N_2 flow.

The aqueous precursor solution was obtained using nickel nitrate salt ($Ni(NO_3)_2.6H_2O$). To fabricate 5 wt. % doped M:NiO thin films, specific amounts of different salts, $Co(NO_3)_2.6H_2O$ and $Mn(NO_3)_2.4H_2O$ were added to the precursor solution. Firstly, 1.454 g of ($Ni(NO_3)_2.6H_2O$)

was dissolved in 100 ml of ethanol to prepare NiO salt solution, and it was directly used for NiO deposition. To prepare Mn and Co-doped NiO precursor solutions, 0.076 g of $Mn(NO_3)_2.4H_2O$ and 0.072 g of $Co(NO_3)_2.6H_2O$ were added into 100 ml of NiO salt solution, respectively. The precursor solutions were sprayed onto glass and ITO/glass substrates using a commercial USD system (Exacta Coat, Sono-Tek) using the ultrasonic Vortex nozzle (operated at 120 kHz), which produces stable and conical spray patterns onto pre-heated substrates (T = 120 °C). The distance between samples and the spraying nozzle was 5.5 cm. The solution flow rate was set at 0.15 ml/min, and clean air was used as a carrier gas at 5 kPa. The ultrasonic nozzle was moved with a constant speed of 40 mm/s in x-y directions following an S-shaped pattern with a spacing of 2 mm. Following deposition, all films were annealed at 350 °C for 90 min under ambient conditions.

2.3. Characterization of Thin Films

2.3.1. Structural characterizations

The crystal structure of the deposited films was examined using Rigaku D/Max-2000 diffractometer with Cu Kα radiation operating at 40 kV (at a wavelength of 0.154 nm) from 10° to 70° at a scan rate of 0.5°/min. X-ray photoelectron spectroscopy (XPS) was used to examine the oxidation state of the elements present in the deposited films. XPS was conducted using a SPECS PHOIBOS hemispherical energy analyzer with a monochromatic Al Kα X-ray excitation source (14 kV, 350 W). The nominal binding energy (B.E.) of the C 1s signal at 284.8 eV was used as a B.E. reference. A spectroscopic ellipsometer was used to determine the thickness of the thin films on a Woollam, M2000V instrument. Data were collected at three different angles of 55, 60, and 65° to improve fitting precision.

2.3.2. Morphological and optical characterization

Scanning electron microscopy (SEM) analyses were conducted to investigate the microstructure of the deposited thin films using an FEI Nova Nano FEG-SEM equipped with a dispersive energy X-ray (EDX) analyzer operated at 20 kV. A thin Au layer was sputtered onto the samples before SEM analysis. Atomic force microscopy (AFM) was used to monitor the surface morphology of the films via a Veeco MultiMode V AFM operated in tapping mode. UV-Visible light transmission of the nanometer-thick films was recorded within 200 - 1000 nm using a PG T80+ UV-Vis Spectrophotometer, where glass substrates were used as a background.

2.3.3. Electrochemical characterization

Electrochemical measurements were performed using a VMP-3 Biologic potentiostat/galvanostat. Cycling voltammetry measurements were conducted in a three-electrode setup, where thin films were working electrodes (with dimensions of 0.8 cm x 1.5 cm), Ag/AgCl (in saturated potassium chloride) was the reference, and Pt foil was the counter electrode. The potential range of CVs varied from -0.2 V to 0.8 V, and the scan rates were 5, 10, 25, 50, and 75 mV/s in an 0.1 M aqueous sodium hydroxide (NaOH) electrolyte. The CVs were compared both in the absence and presence of glucose at a scan rate of 50 mV/s, where 1 ml of 1 mM glucose was added into a 15 ml of 0.1 M NaOH electrolyte, where the final glucose concentration was 62.5 μM. Similarly, a three-electrode setup was built for the amperometric sensor measurements. Ag/AgCl was used as the reference electrode, a Pt wire was used as the counter electrode, and fabricated thin films were used as the working electrodes. Measurements

were conducted using a 0.1 M NaOH electrolyte, where pure nitrogen gas was purged into the electrolyte for a few minutes before measurements. During the glucose sensor measurements, 25 µl of 1 and 10 mM aqueous glucose solution were added into a 15 ml electrolyte with equal time intervals under constant stirring (500 rpm), and +0.65 V *vs.* Ag/AgCl was applied. Similar to the glucose sensor measurements, H_2O_2 sensor measurements were conducted using the same 3-electrode configuration. 25 µl of 1 and 10 mM H_2O_2 solution were added into 15 ml electrolyte at an applied potential of +0.65 V *vs.* Ag/AgCl. Electrochemical impedance spectroscopy (EIS) measurements were performed with a 5 mV amplitude in the 1 MHz – 0.1 Hz frequency range. Before EIS measurements, the thin film electrodes were stabilized at an applied potential of 0 V (*vs.* Ag/AgCl) for 60 s. In order to determine the electrochemically active surface area (ECSA) of the fabricated electrodes, CV measurements were conducted in 0.2 M KCl solution containing 10 mM $K_4[Fe(CN)_6]$ with different scan rates from 200 mV/s to 10 mV/s within the potential range of 0 - 0.6 V. In all measurements, the geometric area of the electrodes dipped into the electrolyte was fixed to ca. 0.1 cm^2.

2.3.4.Blood serum process

Blood samples were collected into vacuum-sealed centrifuge tubes in Middle East Technical University Medical Centre. Once the blood collection tubes were filled, they were centrifuged at 5000 rpm for 5 min. Then, blood serum was collected and used as a glucose source for amperometric measurements. Amperometric detection of glucose in human serum was followed in a three-electrode setup, where thin films were working electrodes, Ag/AgCl (in saturated potassium chloride) was the reference, and Pt foil was the counter electrode. Measurements were conducted in 0.1 M KOH electrolyte at an applied potential of +0.65 V *vs.* Ag/AgCl under continuous stirring, and 25 µl of human serum was introduced to electrolyte with stepwise addition. Commercial OPTIMA Blood Glucose Meter (Model: OK-10) with strip electrodes (OK Biotech Co., Ltd.) was also used to measure the blood glucose level in comparison.

3. Results and Discussions

The average thicknesses of bare NiO and M:NiO thin films were determined as 140 ± 5 nm via ellipsometry. All films were found to have the same thickness due to the same deposition and annealing conditions. The fitting curves of all thin films and fitting parameters of ellipsometry are provided in **Fig. S1** and **Table S1**, respectively. The Cauch model was followed to determine the thickness of the thin films.

XRD was conducted to reveal the phases and crystallographic information of fabricated bare and doped thin films. XRD patterns of the bare NiO, Mn:NiO, and Co:NiO thin films, provided in **Fig. 1a**, showed that all thin films had a cubic structure of NiO (PDF 00-047-1049). XRD patterns of both bare NiO and doped thin films had distinct diffraction peaks at 2θ values of 37.3°, 43.3° and 62.9° indexed to (111), (200) and (220) planes of cubic NiO structure, respectively. No other peaks for both cobalt oxide and manganese oxide or intermetallics or other impurities were detected, indicating that doping did not change the original cubic NiO structure. On the other hand, no detectable shifts were observed for diffraction peaks of Co:NiO and Mn:NiO thin films compared to bare NiO thin film. In addition, upon doping with Mn and Co, the XRD profile showed a slight increase in the full-width half-maximum (FWHM) value of the thin films. The ionic radii of Ni^{+2}, Mn^{+2}, Mn^{+3} and Mn^{+4} are 0.69 , 0.67 , 0.58 and 0.53 Å, respectively [44]. Due to the smaller ionic radius of Mn ions compared to Ni ion, the substitutional

doping of Mn ion is possible on the Ni ion site. This is also in excellent harmony with the currently reported Mn:NiO studies [45–47]. Similarly, the ionic radii of Co^{2+} is 0.65 Å [48], smaller than Ni^{+2}, which proves substitutional doping [49–51].

The average crystallite sizes, microstrain, and dislocation density values calculated for (111) plane from the XRD profiles are provided in **Table S2**. The average crystallite sizes (D) were found to be 35.4, 33.5, and 30.7 nm for bare NiO, Mn:NiO and Co:NiO, respectively, which were calculated using the Scherrer's equation ($D = 0.94\lambda/\beta\, cos\theta$). Herein, λ refers to the wavelength of the X-ray, β is the FWHM, and θ is the Bragg angle. The crystallite size of Mn:NiO and Co:NiO thin films were observed to be smaller than that of bare NiO thin films. Mn and Co atoms might act as obstacles and prevent the growth of crystallites due to the lattice strain in M:NiO thin films. The microstrain (ε) and dislocation density (δ) were calculated using relations $\varepsilon = \beta/(4\tan\theta)$ [52] and $\delta = 1/D^2$ [53], respectively. Compared to the bare NiO thin films, the dislocation density increases with a reduction in particle size for M:NiO thin films. Since the microstrain generally is at the same trend with dislocation density, it increased as the crystallite size decreased.

X-ray photoelectron spectroscopy (XPS) measurements were conducted to reveal the chemical states of the fabricated bare NiO and doped thin films. **Figs. 1(b-f)** show the high-resolution XPS spectra of the Ni 2p and O 1s. The deconvoluted Ni 2p spectra for all thin films, given in **Fig. 1b**, showed distinctive multiplet-split signals for $2p_{3/2}$ and $2p_{1/2}$ with their corresponding shake-up satellites. The spin-orbit coupling for $2p_{3/2}$ and $2p_{1/2}$ domains correspond to binding energy values in the range of 850-869 eV and 870-885 eV, respectively. There are Satellite 1, Satellite 2 and main peak for $2p_{3/2}$, and Satellite 3 and main peak for $2p_{1/2}$. The Ni $2p_{3/2}$ for bare NiO thin film is centered at 853.6 eV, whereas those for Co and Mn doped NiO thin films are 853.7 and 853.9 eV, respectively. Similarly, the Ni $2p_{1/2}$ for bare NiO thin film is centered at 870.7 eV, whereas those for Co and Mn-doped NiO thin films are at 870.8 and 871.0 eV, respectively. As provided in **Fig. 1c**, there are slight shifts to higher binding energy levels. Ni $2p_{3/2}$ peaks shifted by 0.1 eV for Co:NiO and 0.3 eV for Mn:NiO, which is attributed to the partial substitution of Ni sites in the crystal structure to the dopant atoms. This substitution results in a decrease in the electron density and an increase in the force on electrons by the nucleus. As a result, Ni 2p spectra with doping shift to higher binding energy values compared to that of bare NiO. In addition to Ni^{2+} signals, the shoulders occurred at 855.3, 855.6 and 855.7 eV belong to bare NiO, Co:NiO and Mn:NiO, respectively, due to the presence of a small quantity of Ni^{3+} on the surface as in the form of Ni_2O_3. The deconvoluted spectra of O 1s is provided in Fig. 1b and the peak positions are tabulated and provided in **Table S3**. In all cases, four peaks correspond to lattice oxygen in the form of Ni-O octahedral bonding (Ni^{2+}), lattice oxygen due to the presence of Ni_2O_3 compound (Ni^{3+}), surface hydroxyl groups (–OH) and absorbed molecular oxygen present in deposited thin films. Similar to Ni 2p, there are shifts in the peak positions of lattice oxygen (Ni^{2+}) to higher binding energy values, revealing the electron configuration change. When XPS survey spectra of the bare NiO thin film was examined between the binding energy values of 660-630 eV and 805-775 eV (corresponding to Mn 2p and Co 2p, respectively) the signal levels was found to be at the background level (compared to the signal levels obtained for Mn:NiO and Co:NiO thin films (**Figs. S2 (a) and (b)**)). In addition to Ni 2p and O 1s spectra, deconvoluted XPS spectra of dopant elements (Mn, Co) are provided in **Fig. S2 (c) and (d)**, respectively. As XRD implies that there are no additional phases and dopant atoms placed in the positions of substitutional Ni sites, the XPS

spectra revealed that the surface of the Mn:NiO, and Co:NiO thin films composed of mixed valence compounds, which possessed a composition containing Co^{2+} at 779.8 eV with satellite peak at 783.4 eV for Co:NiO [54] and Mn^{2+} at 637.1 eV, Mn^{3+} at 640.8 eV and Mn^{4+} at 643.6 eV for Mn:NiO [55].

SEM and AFM analyses revealed the surface morphology of the deposited bare NiO and doped thin films (**Fig.2**). SEM image in **Fig. 2a** showed that bare NiO thin film has a relatively smooth surface. This smooth surface has a low root mean square (RMS) roughness value as provided in corresponding 3D AFM maps in **Fig. 2d**. Nanosized, spherical particles started to appear following the addition of Mn and Co dopant atoms, as shown in **Fig. 2b** and **2c**, respectively. No significant cracks were seen for the thin films. Observations of ordered nanostructures in SEM images are consistent with the XRD results (**Fig. 1a**). 3D AFM profiles for bare NiO, Co:NiO and Mn:NiO thin films are provided in **Figs. 2d, 2e and 2f**, respectively. The RMS roughness values for the bare NiO, Mn:NiO, and Co:NiO thin films are determined as 1.4 nm, 16.4 nm, and 10.1 nm, respectively. RMS roughness values of the doped films were found to be higher than that of the bare NiO thin film. In addition to the SEM and AFM analyses, energy dispersive X-ray analysis (EDX) was conducted for further analysis of bare NiO and doped thin film electrodes. EDX results tabulated in **Table S4**, revealed that bare NiO, Mn:NiO, and Co:NiO thin films contain similar Ni (wt. %) content. In addition, Mn:NiO and Co:NiO thin films have 5.82 wt.% of Mn and 5.59 wt.% of Co, respectively.

The optical transmittance of bare NiO and doped thin films within a wavelength range of 300 to 1000 nm is shown in **Fig. 3a**. All fabricated films exhibited high transmittance values above 500 nm wavelength, with average transmittance values lying between 70 % and 95 %. Yet, low optical transmittance was seen near the UV region (300-400 nm) due to the strong absorption behavior of thin films. Upon doping, the transmission of the Co:NiO and Mn:NiO thin films decreased in the visible region compared to the bare NiO thin film**.** The decrease in transmittance for doped thin films may be attributed to the changes in their surface morphology [56]. These findings are in good agreement with the transmittance results for doped NiO thin films in the literature [57,58].

XPS results suggested that the electronic structure of NiO thin films was altered with Co and Mn doping. To confirm the change in electronic structure, one can compare the optical bandgaps of the NiO, Co:NiO, and Mn:NiO thin films. In this regard, the optical bandgap values of all fabricated films were determined via UV-Vis measurements using Tauc's relation,

$$\alpha h\nu = A(h\nu - E_g)^m$$

, where α is the absorption coefficient obtained from Lambert formula, $h\nu$ is the incident photon energy, A is the characteristic constant independent of photon energy, E_g is the optical band gap, and m is an index that can have different values such as $1/2$, $3/2$, 2 or 3 depending on the nature of the electronic transitions. Plot showing the variation of $(\alpha h\nu)^2$ versus $h\nu$ for bare NiO, Mn:NiO, and Co:NiO films are provided in **Fig. 3b**. E_g values of the films were estimated through extrapolating the linear portion of the plots. Bandgap values of 3.74, 3.55, and 3.52 eV were obtained for bare NiO, Mn:NiO, and Co:NiO films, respectively. The reduction in the bandgap due to Mn and Co doping in NiO film may be due to the formation of some additional energy levels in the NiO near the valence band edge, resulting in a reduction of the energy associated with the transition from the valence band to the conduction band [59]. Moreover, it is

related to the structural modifications of NiO upon doping. Previous studies have also reported a decrease in the optical band gap of NiO upon doping [60–62].

The cyclic voltammetry (CV) measurements were conducted to reveal electrocatalytic behaviors of NiO and M:NiO (M = Co, Mn) thin-film electrodes. **Figs. 4(a-c)** show the CV curves of NiO, Co:NiO, and Mn:NiO thin-film electrodes within the potential range of -0.2 V to 0.8 V in 0.1 M NaOH electrolyte. The scan rates were increased from 5 to 75 mV/s. In each measurement, redox peaks were found to occur between Ni^{2+} and Ni^{3+} according to the following reversible reaction:

$$NiO + OH^- \quad \rightleftarrows \quad NiO(OH) + e^-$$

Insets of **Figs. 4(a-c)** showed linear relations between both anodic and cathodic peak currents with the square root of scan rates. These results indicated that the redox reaction is a diffusion-controlled electrochemical process, where the diffusion of glucose dominates the electrocatalytic reaction. **Figs. 4(d-f)** show the CV comparison of NiO, Co:NiO, and Mn:NiO thin film in the absence and presence of the glucose to investigate the electrocatalytic activity of the thin films towards glucose. The reactions in the presence of the glucose in the electrolyte are as follows [63]:

$$NiO + OH^- \quad \rightleftarrows \quad NiO(OH) + e^-$$

$$NiO(OH) + Glucose \quad \rightleftarrows \quad NiO + H_2O_2 + Gluconolactone$$

During the CV measurements, Ni^{2+} oxidized to Ni^{3+} due to aqueous electrolyte, and Ni^{3+} acted as catalyst for glucose. Glucose was oxidized by reducing Ni^{3+} to Ni^{2+}. Upon the formation of gluconolactone, it was rapidly converted into gluconic acid, which reacted with water molecules to form hydronium ions (H^+). Upon adding glucose into the electrolyte, there occurred significant enhancements in both anodic and cathodic peak current values and slight shifts towards more positive glucose oxidation potentials. Initially, there was a dynamic balance in Ni^{3+}, Ni^{2+} and hydroxyl ions at the anodic peak potential. Then, a new balance occurred at the electrode and electrolyte interface with the reaction between Ni^{2+} and hydroxyl ions as Ni^{3+} was consumed by glucose. a more anodic potential was required to form Ni^{3+}, due to the presence of hydroxyl concentration polarization [64]. In **Figs. 4 (d-f)**, the oxidation of Ni^{2+} occurs at ca. 0.65 V vs. Ag/AgCl both in the absence and presence of glucose for all thin-film electrodes. Therefore, amperometric biosensor measurements, for both glucose and H_2O_2 sensors, were conducted at an applied potential of 0.65 V vs. Ag/AgCl.

Electrochemical impedance spectroscopy (EIS) was conducted to reveal the performance of the thin-film electrodes. The Nyquist plots of NiO, Co:NiO, and Mn:NiO thin-film electrodes are provided in **Fig. S3**. Within the high-frequency region, they had similar bulk electrolyte resistance and resistance of the electrodes [65]. On the other hand, within the low-frequency region, the presence of the non-vertical lines was assigned to ion transport limitation in the bulk electrolyte to electrode surface [65]. Therefore, electrochemical measurements using NiO, Co:NiO, and Mn:NiO thin films were diffusion-limited.

Electrochemical active surface area (ECSA) of the thin film electrodes were calculated using Randles-Sevcik equation:

$$i_p = 2.686 \times 10^5 \times n^{3/2} \times A \times D^{1/2} \times C \times \vartheta^{1/2}$$

, where i is the peak current (A), n is the number of electrons transferred, A is the electrode area (cm^2), D is the diffusion coefficient (cm^2/s) (6.5 x 10^{-6} cm^2/s for $K_4[Fe(CN)_6]$) (Electrolyte: 0.2 M KCl solution containing 10 mM $K_4[Fe(CN)_6]$), C the concentration (mol/cm^3) and ϑ is the scan rate (V/s). From the **Fig. S4a**, increase in the area of the CV curve at 50 mV/s scan rate indicates that the doping elements, both Co and Mn, enhance the electroactive surface area. From the slope of the peak current vs square root of scan rate graph shown in **Fig. S4b** calculated ECSA values according to the Randles-Sevcik equation were 0.1094 cm^2 for NiO, 0.1223 cm^2 for Co:NiO, and 0.1214 cm^2 for Mn:NiO thin films. This highlighted the improvement of sensor response with the increase in ECSA, thanks to Co and Mn doping elements.

Non-enzymatic glucose sensor measurements were conducted using bare and doped NiO thin film electrodes using constant potential chronoamperometric detection. It was previously reported that doping NiO with transition metals changes the electronic structure of the NiO and enhance its electrocatalytic activity due to the formation of non-stoichiometric compounds [66–68]. **Fig. 5** shows the schematic illustration of the reactions that occur during amperometric glucose sensing, where reactions were explained in detail for CV measurements. **Fig. 6a** shows the amperometric current responses of the NiO, Co:NiO, and Mn:NiO thin-film electrodes to the successive addition of glucose solution at a regular time interval of 100 s. Within the provided concentration range, all thin films started from a similar initial current. Then, upon the addition of glucose solution to electrolyte medium, they gave a stepwise response to the glucose with different current changes. It is obvious in **Fig. 6a** that the current response obtained using NiO thin film is smaller than those with Co:NiO and Mn:NiO thin films. To compare the actual performance of the sensors, in **Fig. 6b**, calibration plots obtained from amperometric current response of the thin film sensors were linearly fitted. The linear regression equations for NiO, Co:NiO and Mn:NiO thin-film sensors were determined $j(\mu A/cm^2) = 4.55+0.44\times[Glucose]/\mu M$ (with correlation coefficient of $R^2 = 0.9986$), $j(\mu A/cm^2) = 3.63+1.67\times[Glucose]/\mu M$ ($R^2 = 0.9998$) and $j(\mu A/cm^2) = 5.44+1.23\times[Glucose]/\mu M$ ($R^2 = 0.9994$), respectively. The sensitivities of the sensors, obtained from the slopes of the regression equations were 0.44 $\mu A/\mu M\cdot cm^2$ for NiO, 1.67 $\mu A/\mu M\cdot cm^2$ for Co:NiO, and 1.23 $\mu A/\mu M\cdot cm^2$ for Mn:NiO thin-film sensors. The limit of detection (LOD) was calculated based on 3×S/N, where S was the standard deviation of fitting and N was the slope of the fitting line. LOD values were 623 nM, 231 nM and 404 nM for NiO, Co:NiO, and Mn:NiO thin film sensors, respectively. The response time of the fabricated thin-film sensors was determined as 8.3 s, 5.4 s, and 6.4 s using 90% of the initial step change in the current and the response times for NiO, Co:NiO, and Mn:NiO thin film sensors, respectively. NiO-based amperometric glucose sensors reported in literature are compared to the fabricated NiO, Co:NiO, and Mn:NiO thin film sensors in this work in Table 1. Considering the amperometric thin-film sensor results, best performance was obtained from Co:NiO thin films compared to NiO and Mn:NiO thin films in terms of sensitivity, LOD, and response time. The enhanced glucose sensing performance was achieved by doping with Mn and Co because the doping altered the electronic structure of the NiO thin films. This led to an increase in the electrocatalytic performance on glucose.

A large-area Co:NiO thin film (15 cm × 15 cm), as shown in **Fig. S5**, was deposited and cut into sensor electrodes. Amperometric measurements were conducted using randomly selected five different Co:NiO thin-film electrodes at an applied potential of 0.65 V (*vs.* Ag/AgCl) upon successive addition of 1 mM glucose. **Fig. 6d** shows the reproducibility of the electrodes with

bar charts corresponding to the amperometric current responses of each electrode, where similar current responses were obtained. The stability of Co:NiO thin film electrode was also studied with five successive amperometric measurements on a single electrode. **Fig. 6e** shows the current response achieved at each step for the five different measurements. After over 10000 s of measurement, the response current to the addition of 25 µl of 1 mM glucose solution at an applied potential of 0.65 V (*vs.* Ag/AgCl) only decreased by 5 %, which proved the long term stability of the Co:NiO thin-film electrode (**Fig. S6 (a)**). In addition, the photographs of Co:NiO thin-film electrode before and after amperometric long term stability test are shown in **Fig. S6 (b)**. Only minor deviations between each measurement were observed. Glucose sensor utilization in practical applications for daily use and clinical analysis was demonstrated using human blood serum. The amperometric measurement with Co:NiO thin-film electrode was conducted by adding 25 µl of blood serum samples to 0.1 M NaOH electrolyte under 0.65V (*vs.* Ag/AgCl), as provided in **Fig. 6f**. The glucose concentration in human blood serum was derived as 143 mg/dl using the linear regression equation for Co:NiO thin-film sensor in Figure 3b. The glucose concentration in the human body was measured as 158 mg/dl with a commercial sensor (**Fig. S7** shows a photo of the commercial sensor and strip showing the recorded measurement), and the Co:NiO thin-film electrode showed 90.1 % accuracy. These and other results obtained in this work demonstrated that the Co:NiO thin-film electrodes, fabricated through the USD method, can be utilized to mass-produce non-enzymatic glucose biosensors.

H_2O_2 biosensors were fabricated to demonstrate the enhanced multifunctional biosensor properties of nanometer-thick NiO electrodes with doping. H_2O_2 is a byproduct of many enzymatic reactions such as oxidation of glucose, alcohol, cholesterol and lactate through the methabolic patways. In addition, H_2O_2 is widely present in the food, textile and pharmaceutical industries. Therefore, detection of H_2O_2 plays an essential role in health monitoring and quality control in various fields[69]. Bare and doped NiO thin-film electrodes were also utilized as non-enzymatic H_2O_2 sensors. The amperometric responses of the electrodes were measured in 0.1 M NaOH electrolyte by the successive addition of H_2O_2. The electrodes were subjected to a constant applied potential of 0.65 V (vs. Ag/AgCl) during the measurements. Under the applied potential, the electrochemical reactions that take place on the NiO surface is provided as below [48]:

$$NiO + OH^- \rightarrow NiOOH + e^-$$

$$NiOOH + H_2O_2 \rightarrow 2NiO + 2H_2O + O_2$$

Fig. 7a shows the amperometric current responses of the NiO, Co:NiO, and Mn:NiO thin-film electrodes for the addition of 25 µl of 1 mM H_2O_2. For all electrodes, a sharp increase in the current response was observed upon the addition of H_2O_2. Starting from a similar initial current, each electrode gave a different current response upon H_2O_2 addition. In **Fig. 7a**, it is shown that NiO thin film electrode gave the weakest current response than Co:NiO and Mn:NiO thin film electrodes, with Mn:NiO thin film showing the strongest current response. Corresponding calibration plots were linearly fitted to characterize further and compare the thin film electrodes, as shown in **Fig. 7b**. The linear regression equations for NiO, Co:NiO and Mn:NiO thin-film sensors were determined as $j(\mu A/cm^2) = 0.012+0.007\times[H_2O_2]/\mu M$ ($R^2 = 0.9967$), $j(\mu A/cm^2) = 0.013+0.011\times[H_2O_2]/\mu M$ ($R^2 = 0.9975$) and $j(\mu A/cm^2) = 0.012+0.012\times[H_2O_2]/\mu M$ ($R^2 = 0.9964$), respectively. Sensitivities of the sensors, obtained from the slope of the regression equations were 0.007 $\mu A/\mu M\cdot cm^2$ for NiO, 0.011 $\mu A/\mu M\cdot cm^2$ for Co:NiO, and 0.012

$\mu A/\mu M \cdot cm^2$ for Mn:NiO thin-film electrodes. In addition, LOD (S/N=3) values were 635 nM, 558 nM and 664 nM for NiO, Co:NiO, and Mn:NiO thin-film sensors, respectively. The response times of the fabricated sensors (according to the 90% of the initial step change in the current response) were 4.7 s, 2.9 s, and 2.4 s for NiO, Co:NiO, and Mn:NiO thin-film sensors, respectively. Considering the performance of the sensors in terms of their sensitivities, LODs, and response times, both Co:NiO and Mn:NiO thin-film sensors showed higher performance than bare NiO thin-film sensors. The improved sensor performance with doping was again attributed to the change in the electronic structure of NiO. A performance comparison table for the fabricated NiO, Co:NiO, and Mn:NiO thin-film sensors to those H_2O_2 biosensor studies in the literature is prepared and provided as **Table 2**. Amperometric measurements were also conducted with 10 mM of H_2O_2 addition, results of which are provided in the inset of **Fig. 7c**. Higher current values were obtained for all thin-film electrodes upon using a higher concentration of H_2O_2 solution, since there were more ions in the electrolyte. Calibration plots, shown in **Fig. 7c**, based on the amperometric measurements of NiO, Co:NiO, and Mn:NiO thin-film electrodes, showed wider linear ranges obtained through the use of high concentration H_2O_2 solution. The linear range was 16-415 μM for NiO, 16-307 μM for Co:NiO, and 16-276 μM for Mn:NiO. For all electrodes, a linear behavior was observed on the calibration plots. However, a decrease in the signal-to-noise ratio drastically affected the quality of the sensor response as the concentration of the H_2O_2 in the electrolyte increased. Similar to the glucose-sensing, there was an improved electrocatalytic performance towards H_2O_2 detection due to the altered electronic structure of NiO by doping with Co and Mn. To determine the selectivity of the Co:NiO thin-film electrode against different interferences, various analytes were introduced during the amperometric measurements, as shown in **Fig. 7d**. Measurements were conducted in 0.1 M NaOH with an applied potential of 0.65 V (vs. Ag/AgCl). The highest response was achieved upon the addition of 10 mM H_2O_2, following that the electrode provided a significant response to the addition of 10 mM glucose. In addition to that, current density values slightly increased upon adding 10 mM urea and 10 mM ascorbic acid. Nevertheless, distinguishable current responses were recorded for H_2O_2 (Δj: 3.69 $\mu A/cm^2$) and glucose (Δj: 1.39 $\mu A/cm^2$) as the height difference between steps toward introduction of H_2O_2 and glucose. On the other hand, the thin film sensor did not respond to adding 10 mM lactic acid and 10 mM oxalic acid. Distinct current responses toward each analyte indicated the efficient analyte selectivity of the Co:NiO thin film electrode.

4. Conclusions

This work covered the deposition of bare NiO and M:NiO (Co, Mn) nanometer-thick thin films onto ITO/glass substrates through the USD method. The XPS results revealed that electronic structure of NiO was altered through doping with Co and Mn, which resulted in improved electrocatalytic activity. The functional thin films were utilized as high-performance non-enzymatic both glucose and as well as H_2O_2 biosensor electrodes. Co:NiO nanometer-thick film electrodes showed higher glucose sensor performance than both bare NiO and Mn:NiO electrodes regarding sensitivity, LOD, and response time. The non-enzymatic glucose sensor with Co:NiO thin-film electrodes showed promising analyte selectivity using various interferences. The amperometric performance of randomly selected electrodes that were fabricated through large-area deposition (15 cm x 15 cm) and cut into small electrodes showed coherent reproducibility. Due to the enhancement of the electrocatalytic performance of NiO with doping, non-enzymatic H_2O_2 biosensors were also fabricated and performances of thin-

film electrodes with bare and doped NiO were determined. It was demonstrated that the performance of H_2O_2 sensors with doping was also enhanced. All in all, high-performance non-enzymatic nanometer-thick film biosensors hold great potential to replace commercial sensors, which necessitates an enzyme and suffer from enzyme denaturation. The USD is an excellent method for the large-scale fabrication of thin-film electrodes with good reproducibility in a cost-effective manner under ambient conditions. The doped nanometer-thick film sensors reported in this work are highly promising to be effectively used in actual clinical and daily monitoring applications.

Credit authorship contribution statement

Yusuf Tutel: Conceptualization, Methodology, Formal analysis, Investigation, Writing – original draft, Writing – review & editing, Visualization. **Serkan Koylan:** Conceptualization, Methodology, Formal analysis, Investigation, Writing – original draft, Writing – review & editing, Visualization. **Sensu Tunca:** Conceptualization, Methodology, Writing – original draft. **Husnu Emrah Unalan:** Conceptualization, Supervision, Writing – review & editing, funding acquisition.

Supporting Information

Ellipsometry Fitting, additional X-ray photoelectron spectroscopy (XPS) results, Energy-dispersive X-ray spectroscopy (EDX) results, Nyquist Plot, Electrochemical Active Surface Area (ECSA) Calculation, Photography of Large Area Co:NiO Thin Film, Long Term Stability Test Result and Commercial Glucose Sensor Used in This Work.

References

(1) Wong, T. Y.; Cheung, C. M. G.; Larsen, M.; Sharma, S.; Simó, R. Diabetic Retinopathy. *Nat. Rev. Dis. Prim.* **2016**, *2* (1), 16012. https://doi.org/10.1038/nrdp.2016.12.

(2) Huang, W.; Ding, S.; Chen, Y.; Hao, W.; Lai, X.; Peng, J.; Tu, J.; Cao, Y.; Li, X. 3D NiO Hollow Sphere/Reduced Graphene Oxide Composite for High-Performance Glucose Biosensor. *Sci. Rep.* **2017**, *7* (1), 5220. https://doi.org/10.1038/s41598-017-05528-1.

(3) Yang, W.; Ratinac, K. R.; Ringer, S. R.; Thordarson, P.; Gooding, J. J.; Braet, F. Carbon Nanomaterials in Biosensors: Should You Use Nanotubes or Graphene. *Angew. Chemie - Int. Ed.* **2010**, *49* (12), 2114–2138. https://doi.org/10.1002/anie.200903463.

(4) Toghill, K. E.; Compton, R. G. Electrochemical Non-Enzymatic Glucose Sensors: A Perspective and an Evaluation. *Int. J. Electrochem. Sci.* **2010**, *5* (9), 1246–1301.

(5) Ju, J.; Chen, W. In Situ Growth of Surfactant-Free Gold Nanoparticles on Nitrogen-Doped Graphene Quantum Dots for Electrochemical Detection of Hydrogen Peroxide in Biological Environments. *Anal. Chem.* **2015**, *87* (3), 1903–1910. https://doi.org/10.1021/ac5041555.

(6) Kang, X.; Mai, Z.; Zou, X.; Cai, P.; Mo, J. A Sensitive Non-enzymatic Glucose Sensor in Alkaline Media with a Copper Nanocluster/Multiwall Carbon Nanotube-Modified Glassy Carbon Electrode. *Anal. Biochem.* **2007**, *363* (1), 143–150. https://doi.org/10.1016/j.ab.2007.01.003.

(7) Ding, L.; Yan, F.; Zhang, Y.; Liu, L.; Yu, X.; Liu, H. Microflowers Comprised of Cu/CuxO/NC Nanosheets as Electrocatalysts and Horseradish Peroxidase Mimics. *ACS Appl. Nano Mater.* **2020**, *3* (1), 617–623. https://doi.org/10.1021/acsanm.9b02156.

(8) Lu, L. M.; Zhang, L.; Qu, F. L.; Lu, H. X.; Zhang, X. B.; Wu, Z. S.; Huan, S. Y.; Wang, Q. A.; Shen, G. L.; Yu, R. Q. A Nano-Ni Based Ultrasensitive Non-enzymatic Electrochemical Sensor for Glucose: Enhancing Sensitivity through a Nanowire Array Strategy. *Biosens. Bioelectron.* **2009**, *25* (1), 218–223. https://doi.org/10.1016/j.bios.2009.06.041.

(9) Ibupoto, Z. H.; Khun, K.; Lu, J.; Willander, M. The Synthesis of CuO Nanoleaves, Structural Characterization, and Their Glucose Sensing Application. *Appl. Phys. Lett.* **2013**, *102* (10), 103701. https://doi.org/10.1063/1.4795135.

(10) Si, P.; Ding, S.; Yuan, J.; Lou, X. W.; Kim, D. H. Hierarchically Structured One-Dimensional TiO2 for Protein Immobilization, Direct Electrochemistry, and Mediator-Free Glucose Sensing. *ACS Nano* **2011**, *5* (9), 7617–7626. https://doi.org/10.1021/nn202714c.

(11) Cheng, X.; Zhang, S.; Zhang, H.; Wang, Q.; He, P.; Fang, Y. Determination of Carbohydrates by Capillary Zone Electrophoresis with Amperometric Detection at a Nano-Nickel Oxide Modified Carbon Paste Electrode. *Food Chem.* **2008**, *106* (2), 830–835. https://doi.org/10.1016/j.foodchem.2007.06.063.

(12) Sedaghat, S.; Piepenburg, C. R.; Zareei, A.; Qi, Z.; Peana, S.; Wang, H.; Rahimi, R. Laser-Induced Mesoporous Nickel Oxide as a Highly Sensitive Non-enzymatic Glucose Sensor. *ACS Appl. Nano Mater.* **2020**, *3* (6), 5260–5270. https://doi.org/10.1021/acsanm.0c00659.

(13) Borade, P. A.; Ali, M. A.; Jahan, S.; Sant, T.; Bogle, K.; Panat, R.; Jejurikar, S. M. MoS2Nanosheet-Modified NiO Layers on a Conducting Carbon Paper for Glucose Sensing. *ACS Appl. Nano Mater.* **2021**, *4* (7), 6609–6619. https://doi.org/10.1021/acsanm.1c00122.

(14) Casella, I. G. Electrodeposition of Cobalt Oxide Films from Carbonate Solutions Containing Co(II)-Tartrate Complexes. *J. Electroanal. Chem.* **2002**, *520* (1–2), 119–125. https://doi.org/10.1016/S0022-0728(02)00642-3.

(15) Mu, Y.; Jia, D.; He, Y.; Miao, Y.; Wu, H. L. Nano Nickel Oxide Modified Non-Enzymatic Glucose Sensors with Enhanced Sensitivity through an Electrochemical Process Strategy at High Potential. *Biosens. Bioelectron.* **2011**, *26* (6), 2948–2952. https://doi.org/10.1016/j.bios.2010.11.042.

(16) Park, S.; Boo, H.; Chung, T. D. Electrochemical Non-Enzymatic Glucose Sensors. *Anal. Chim. Acta* **2006**, *556* (1), 46–57. https://doi.org/10.1016/j.aca.2005.05.080.

(17) Prasad, R.; Bhat, B. R. Multi-Wall Carbon Nanotube-NiO Nanoparticle Composite as Enzyme-Free Electrochemical Glucose Sensor. *Sensors Actuators, B Chem.* **2015**, *220*, 81–90. https://doi.org/10.1016/j.snb.2015.05.065.

(18) Sun, Y.; Buck, H.; Mallouk, T. E. Combinatorial Discovery of Alloy Electrocatalysts for Amperometric Glucose Sensors. *Anal. Chem.* **2001**, *73* (7), 1599–1604. https://doi.org/10.1021/ac0015117.

(19) Singh, B.; Laffir, F.; McCormac, T.; Dempsey, E. PtAu/C Based Bimetallic Nanocomposites for Non-Enzymatic Electrochemical Glucose Detection. *Sensors Actuators, B Chem.* **2010**, *150* (1), 80–92. https://doi.org/10.1016/j.snb.2010.07.039.

(20) Raymundo-Pereira, P. A.; Shimizu, F. M.; Coelho, D.; Piazzeta, M. H. O.; Gobbi, A. L.; Machado, S. A. S.; Oliveira, O. N. A Nanostructured Bifunctional Platform for Sensing of Glucose Biomarker in Artificial Saliva: Synergy in Hybrid Pt/Au Surfaces. *Biosens. Bioelectron.* **2016**, *86*, 369–376. https://doi.org/10.1016/j.bios.2016.06.053.

(21) Koylan, S.; Tunca, S.; Polat, G.; Durukan, M. B.; Kim, D.; Kalay, Y. E.; Ko, S. H.; Unalan, H. E. Highly Stable Silver-Platinum Core-Shell Nanowires for H2O2detection. *Nanoscale* **2021**, *13* (30), 13129–13141. https://doi.org/10.1039/d1nr01976g.

(22) Pötzelberger, I.; Mardare, A. I.; Hassel, A. W. Non-Enzymatic Glucose Sensing on Copper-Nickel Thin Film Alloy. *Appl. Surf. Sci.* **2017**, *417*, 48–53. https://doi.org/10.1016/j.apsusc.2016.12.193.

(23) Xu, C.; Liu, Y.; Su, F.; Liu, A.; Qiu, H. Nanoporous PtAg and PtCu Alloys with Hollow Ligaments for Enhanced Electrocatalysis and Glucose Biosensing. *Biosens. Bioelectron.* **2011**, *27* (1), 160–166. https://doi.org/10.1016/j.bios.2011.06.036.

(24) Chowdhury, M.; Ossinga, C.; Cummings, F.; Chamier, J.; Kebede, M. Novel Sn Doped Co3O4 Thin Film for Non-enzymatic Glucose Bio-Sensor and Fuel Cell. *Electroanalysis* **2017**, *29* (8), 1876–1886. https://doi.org/10.1002/elan.201700184.

(25) Tian, H.; Jia, M.; Zhang, M.; Hu, J. Non-enzymatic Glucose Sensor Based on Nickel Ion Implanted-Modified Indium Tin Oxide Electrode. *Electrochim. Acta* **2013**, *96*, 285–290. https://doi.org/10.1016/j.electacta.2013.02.096.

(26) Roushani, M.; Abdi, Z.; Daneshfar, A.; Salimi, A. Hydrogen Peroxide Sensor Based on Riboflavin Immobilized at the Nickel Oxide Nanoparticle-Modified Glassy Carbon Electrode. *J. Appl. Electrochem.* **2013**, *43* (12), 1175–1183. https://doi.org/10.1007/s10800-013-0603-9.

(27) Vadnala, S.; Tripathy, S.; Paul, N.; Agrawal, A.; Singh, S. G. Facile Synthesis of Electrospun Nickel (II) Oxide Nanofibers and Its Application for Hydrogen Peroxide Sensing. *ChemistrySelect* **2018**, *3* (43), 12263–12268. https://doi.org/10.1002/slct.201802526.

(28) Ojani, R.; Raoof, R. O.; Norouzi, B. An Efficient Sensor for Determination of Concentrated Hydrogen Peroxide Based on Nickel Oxide Modified Carbon Paste Electrode. *Int. J. Electrochem. Sci.* **2012**, *7* (3), 1852–1863.

(29) Wang, Z.; Hu, Y.; Yang, W.; Zhou, M.; Hu, X. Facile One-Step Microwave-Assisted Route towards Ni Nanospheres/Reduced Graphene Oxide Hybrids for Non-Enzymatic Glucose Sensing. *Sensors* **2012**, *12* (4), 4860–4869. https://doi.org/10.3390/s120404860.

(30) Wang, J.; Bao, W.; Zhang, L. A Non-enzymatic Glucose Sensing Platform Based on Ni Nanowire Modified Electrode. *Anal. Methods* **2012**, *4* (12), 4009–4013. https://doi.org/10.1039/c2ay25759a.

(31) Wang, B.; Li, S.; Liu, J.; Yu, M. Preparation of Nickel Nanoparticle/Graphene Composites for Nonenzymatic Electrochemical Glucose Biosensor Applications. *Mater. Res. Bull.* **2014**, *49* (1), 521–524. https://doi.org/10.1016/j.materresbull.2013.08.066.

(32) Xiao, X.; Michael, J. R.; Beechem, T.; McDonald, A.; Rodriguez, M.; Brumbach, M. T.; Lambert, T. N.; Washburn, C. M.; Wang, J.; Brozik, S. M.; Wheeler, D. R.; Burckel, D. B.; Polsky, R. Three Dimensional Nickel-Graphene Core-Shell Electrodes. *J. Mater. Chem.* **2012**, *22* (45), 23749–23754. https://doi.org/10.1039/c2jm35506j.

(33) Martins, T. S.; Bott-Neto, J. L.; Raymundo-Pereira, P. A.; Ticianelli, E. A.; Machado, S. A. S. An Electrochemical Furosemide Sensor Based on Pencil Graphite Surface Modified with Polymer Film Ni-Salen and Ni(OH)2/C Nanoparticles. *Sensors Actuators B Chem.* **2018**, *276*, 378–387. https://doi.org/10.1016/j.snb.2018.08.131.

(34) Raymundo-Pereira, P. A.; Lima, A. R. F.; Machado, S. A. S. A Nanostructured Label-Free Platform Based on an Ultrathin Film for Ultrasensitive Detection of a Secosteroid Hormone. *RSC Adv.* **2016**, *6* (41), 34458–34467. https://doi.org/10.1039/C6RA04740H.

(35) Ding, Y.; Liu, Y.; Parisi, J.; Zhang, L.; Lei, Y. A Novel NiO-Au Hybrid Nanobelts Based Sensor for Sensitive and Selective Glucose Detection. *Biosens. Bioelectron.* **2011**, *28* (1), 393–398. https://doi.org/10.1016/j.bios.2011.07.054.

(36) Gao, J.; Meng, T.; Lu, S.; Ma, X.; Zhang, Y.; Fu, D.; Lu, Z.; Li, C. M. Manganese-Doped Tremella-like Nickel Oxide as Biomimetic Sensors toward Highly Sensitive Detection of Glucose in Human Serum. *J. Electroanal. Chem.* **2020**, *863*, 114071. https://doi.org/10.1016/j.jelechem.2020.114071.

(37) Jana, S.; Mondal, G.; Mitra, B. C.; Bera, P.; Chakraborty, B.; Mondal, A.; Ghosh, A. Facile Synthesis of Nickel Oxide Thin Films from PVP Encapsulated Nickel Sulfide Thin Films: An Efficient Material for Electrochemical Sensing of Glucose, Hydrogen Peroxide and Photodegradation of Dye. *New J. Chem.* **2017**, *41* (24), 14985–14994. https://doi.org/10.1039/c7nj02985c.

(38) Tyagi, M.; Tomar, M.; Gupta, V. Influence of Hole Mobility on the Response Characteristics of P-Type Nickel Oxide Thin Film Based Glucose Biosensor. *Anal. Chim. Acta* **2012**, *726*, 93–101. https://doi.org/10.1016/j.aca.2012.03.027.

(39) Garcia-Garcia, F. J.; Salazar, P.; Yubero, F.; González-Elipe, A. R. Non-Enzymataic Glucose Electrochemical Sensor Made of Porous NiO Thin Films Prepared by Reactive Magnetron Sputtering at Oblique Angles. *Electrochim. Acta* **2016**, *201*, 38–44. https://doi.org/10.1016/j.electacta.2016.03.193.

(40) Raza, M. H.; Movlaee, K.; Wu, Y.; El-Refaei, S. M.; Karg, M.; Leonardi, S. G.; Neri, G.; Pinna, N. Tuning the NiO Thin Film Morphology on Carbon Nanotubes by Atomic Layer Deposition for Enzyme-Free Glucose Sensing. *ChemElectroChem* **2019**, *6* (2), 383–392. https://doi.org/10.1002/celc.201801420.

(41) Singer, N.; Pillai, R. G.; Johnson, A. I. D.; Harris, K. D.; Jemere, A. B. Nanostructured Nickel Oxide Electrodes for Non-Enzymatic Electrochemical Glucose Sensing. *Microchim. Acta* **2020**, *187* (4), 196. https://doi.org/10.1007/s00604-020-4171-5.

(42) Jana, S.; Samai, S.; Mitra, B. C.; Bera, P.; Mondal, A. Nickel Oxide Thin Film from Electrodeposited Nickel Sulfide Thin Film: Peroxide Sensing and Photo-

Decomposition of Phenol. *Dalt. Trans.* **2014**, *43* (34), 13096–13104. https://doi.org/10.1039/c4dt01658k.

(43) Salazar, P.; Rico, V.; González-Elipe, A. R. Non-Enzymatic Hydrogen Peroxide Detection at NiO Nanoporous Thin Film- Electrodes Prepared by Physical Vapor Deposition at Oblique Angles. *Electrochim. Acta* **2017**, *235*, 534–542. https://doi.org/10.1016/j.electacta.2017.03.087.

(44) Shannon, R. D. Revised Effective Ionic Radii and Systematic Studies of Interatomic Distances in Halides and Chalcogenides. *Acta Crystallogr. Sect. A* **1976**, *32* (5), 751–767. https://doi.org/10.1107/S0567739476001551.

(45) Patel, K. N.; Deshpande, M. P.; Chauhan, K.; Rajput, P.; Gujarati, V. P.; Pandya, S.; Sathe, V.; Chaki, S. H. Effect of Mn Doping Concentration on Structural, Vibrational and Magnetic Properties of NiO Nanoparticles. *Adv. Powder Technol.* **2018**, *29* (10), 2394–2403. https://doi.org/10.1016/j.apt.2018.06.018.

(46) Thangamani, C.; Vijaya Kumar, P.; Gurushankar, K.; Pushpanathan, K. Structural and Size Dependence Magnetic Properties of Mn-Doped NiO Nanoparticles Prepared by Wet Chemical Method. *J. Mater. Sci. Mater. Electron.* **2020**, *31* (14), 11101–11112. https://doi.org/10.1007/s10854-020-03659-2.

(47) Layek, S.; Verma, H. C. Room Temperature Ferromagnetism in Mn-Doped NiO Nanoparticles. *J. Magn. Magn. Mater.* **2016**, *397*, 73–78. https://doi.org/10.1016/j.jmmm.2015.08.082.

(48) Yu, Z.; Li, H.; Zhang, X.; Liu, N.; Zhang, X. NiO/Graphene Nanocomposite for Determination of Hwith a Low Detection Limit. *Talanta* **2015**, *144*, 1–5. https://doi.org/10.1016/j.talanta.2015.05.070.

(49) Xu, H.; Zeng, M.; Li, J.; Tong, X. Facile Hydrothermal Synthesis of Flower-like Co-Doped NiO Hierarchical Nanosheets as Anode Materials for Lithium-Ion Batteries. *RSC Adv.* **2015**, *5* (111), 91493–91499. https://doi.org/10.1039/c5ra17017f.

(50) Xue, J.; Li, W.; Song, Y.; Li, Y.; Zhao, J. Visualization Electrochromic-Supercapacitor Device Based on Porous Co Doped NiO Films. *J. Alloys Compd.* **2021**, *857*, 158087. https://doi.org/10.1016/j.jallcom.2020.158087.

(51) Qian, J.; Guo, X.; Wang, T.; Liu, P.; Zhang, H.; Gao, D. Bifunctional Porous Co-Doped NiO Nanoflowers Electrocatalysts for Rechargeable Zinc-Air Batteries. *Appl. Catal. B Environ.* **2019**, *250*, 71–77. https://doi.org/10.1016/j.apcatb.2019.03.021.

(52) Sen, S.; Halder, S. K.; Sen, G. S. P. An X-Ray Line Broadening Analysis in the Vacuum-Evaporated Silver Films. *J. Phys. Soc. Japan* **1975**, *38* (6), 1641–1647. https://doi.org/10.1143/JPSJ.38.1641.

(53) Williamson, G. K.; Smallman, R. E. III. Dislocation Densities in Some Annealed and Cold-Worked Metals from Measurements on the X-Ray Debye-Scherrer Spectrum. *Philos. Mag.* **1956**, *1* (1), 34–46. https://doi.org/10.1080/14786435608238074.

(54) Gao, L.; Han, E.; He, Y.; Du, C.; Liu, J.; Yang, X. Effect of Different Templating Agents on Cobalt Ferrite (CoFe2O4) Nanomaterials for High-Performance Supercapacitor. *Ionics (Kiel).* **2020**, *26* (7), 3643–3654. https://doi.org/10.1007/s11581-020-03482-z.

(55) Chen, J.; Zhu, B.; Sun, Y.; Yin, S.; Zhu, Z.; Li, J. Investigation of Low-Temperature

Selective Catalytic Reduction of NOx with Ammonia over Mn-Modified Fe2O3/AC Catalysts. *J. Braz. Chem. Soc.* **2018**, *29* (1), 79–87. https://doi.org/10.21577/0103-5053.20170116.

(56) Sharma, R.; Acharya, A. D.; Moghe, S.; Shrivastava, S. B.; Gangrade, M.; Shripathi, T.; Ganesan, V. Effect of Cobalt Doping on Microstructural and Optical Properties of Nickel Oxide Thin Films. *Mater. Sci. Semicond. Process.* **2014**, *23* (1), 42–49. https://doi.org/10.1016/j.mssp.2014.02.004.

(57) Taşköprü, T.; Bayansal, F.; Şahin, B.; Zor, M. Structural and Optical Properties of Co-Doped NiO Films Prepared by SILAR Method. *Philos. Mag.* **2015**, *95* (1), 32–40. https://doi.org/10.1080/14786435.2014.984788.

(58) Chen, S. C.; Kuo, T. Y.; Lin, Y. C.; Lin, H. C. Preparation and Properties of P-Type Transparent Conductive Cu-Doped NiO Films. *Thin Solid Films* **2011**, *519* (15), 4944–4947. https://doi.org/10.1016/j.tsf.2011.01.058.

(59) Owings, R. R.; Exarhos, G. J.; Windisch, C. F.; Holloway, P. H.; Wen, J. G. Process Enhanced Polaron Conductivity of Infrared Transparent Nickel-Cobalt Oxide. *Thin Solid Films* **2005**, *483* (1–2), 175–184. https://doi.org/10.1016/j.tsf.2005.01.011.

(60) Moghe, S.; Acharya, A. D.; Panda, R.; Shrivastava, S. B.; Gangrade, M.; Shripathi, T.; Ganesan, V. Effect of Copper Doping on the Change in the Optical Absorption Behaviour in NiO Thin Films. *Renew. Energy* **2012**, *46*, 43–48. https://doi.org/10.1016/j.renene.2012.02.028.

(61) Sheena, P. A.; Hitha, H.; Sreedevi, A.; Varghese, T. Microstructural Characterization and Modified Spectral Response of Cobalt Doped NiO Nanoparticles. *Mater. Chem. Phys.* **2019**, *229*, 412–420. https://doi.org/10.1016/j.matchemphys.2019.03.033.

(62) Manouchehri, I.; AlShiaa, S. A. O.; Mehrparparvar, D.; Hamil, M. I.; Moradian, R. Optical Properties of Zinc Doped NiO Thin Films Deposited by RF Magnetron Sputtering. *Optik (Stuttg).* **2016**, *127* (20), 9400–9406. https://doi.org/10.1016/j.ijleo.2016.06.092.

(63) Mishra, S.; Yogi, P.; Sagdeo, P. R.; Kumar, R. Mesoporous Nickel Oxide (NiO) Nanopetals for Ultrasensitive Glucose Sensing. *Nanoscale Res. Lett.* **2018**, *13* (1), 16. https://doi.org/10.1186/s11671-018-2435-3.

(64) Guo, C.; Wang, Y.; Zhao, Y.; Xu, C. Non-Enzymatic Glucose Sensor Based on Three Dimensional Nickel Oxide for Enhanced Sensitivity. *Anal. Methods* **2013**, *5* (7), 1644–1647. https://doi.org/10.1039/c3ay00067b.

(65) Mei, B. A.; Munteshari, O.; Lau, J.; Dunn, B.; Pilon, L. Physical Interpretations of Nyquist Plots for EDLC Electrodes and Devices. *J. Phys. Chem. C* **2018**, *122* (1), 194–206. https://doi.org/10.1021/acs.jpcc.7b10582.

(66) Chen, L.; Zhang, H.; Chen, L.; Wei, X.; Shi, J.; He, M. Facile Synthesis of Cu Doped Cobalt Hydroxide (Cu-Co(OH)2) Nano-Sheets for Efficient Electrocatalytic Oxygen Evolution. *J. Mater. Chem. A* **2017**, *5* (43), 22568–22575. https://doi.org/10.1039/c7ta07637a.

(67) Zhang, Y.; Liu, Y.; Ma, M.; Ren, X.; Liu, Z.; Du, G.; Asiri, A. M.; Sun, X. A Mn-Doped Ni2P Nanosheet Array: An Efficient and Durable Hydrogen Evolution Reaction Electrocatalyst in Alkaline Media. *Chem. Commun.* **2017**, *53* (80), 11048–11051.

https://doi.org/10.1039/c7cc06278h.

(68) Liu, T.; Ma, X.; Liu, D.; Hao, S.; Du, G.; Ma, Y.; Asiri, A. M.; Sun, X.; Chen, L. Mn Doping of CoP Nanosheets Array: An Efficient Electrocatalyst for Hydrogen Evolution Reaction with Enhanced Activity at All PH Values. *ACS Catal.* **2017**, *7* (1), 98–102. https://doi.org/10.1021/acscatal.6b02849.

(69) Giaretta, J. E.; Oveissi, F.; Dehghani, F.; Naficy, S. Paper-Based, Chemiresistive Sensor for Hydrogen Peroxide Detection. *Adv. Mater. Technol.* **2021**, *6* (4), 2001148. https://doi.org/10.1002/admt.202001148.

(70) Ci, S.; Huang, T.; Wen, Z.; Cui, S.; Mao, S.; Steeber, D. A.; Chen, J. Nickel Oxide Hollow Microsphere for Non-Enzyme Glucose Detection. *Biosens. Bioelectron.* **2014**, *54*, 251–257. https://doi.org/10.1016/j.bios.2013.11.006.

(71) Zhang, W. De; Chen, J.; Jiang, L. C.; Yu, Y. X.; Zhang, J. Q. A Highly Sensitive Non-enzymatic Glucose Sensor Based on NiO-Modified Multi-Walled Carbon Nanotubes. *Microchim. Acta* **2010**, *168* (3), 259–265. https://doi.org/10.1007/s00604-010-0288-2.

(72) Zhu, J.; Yin, H.; Gong, J.; Al-Furjan, M. S. H.; Nie, Q. Easy One Pot Synthesis of NiO/Nitrogen Doped Carbon Spheres for Highly Sensitive Enzyme Free Amperometric Glucose Sensors. *Appl. Surf. Sci.* **2018**, *444*, 56–64. https://doi.org/10.1016/j.apsusc.2018.02.233.

(73) Zhang, H.; Liu, S. Nanoparticles-Assembled NiO Nanosheets Templated by Graphene Oxide Film for Highly Sensitive Nonenzymatic Glucose Sensing. *Sensors Actuators, B Chem.* **2017**, *238*, 788–794. https://doi.org/10.1016/j.snb.2016.07.126.

(74) Rajendran, S.; Manoj, D.; Raju, K.; Dionysiou, D. D.; Naushad, M.; Gracia, F.; Cornejo, L.; Gracia-Pinilla, M. A.; Ahamad, T. Influence of Mesoporous Defect Induced Mixed-Valent NiO (Ni2+/Ni3+)-TiO2 Nanocomposite for Non-Enzymatic Glucose Biosensors. *Sensors Actuators, B Chem.* **2018**, *264*, 27–37. https://doi.org/10.1016/j.snb.2018.02.165.

(75) Ahmad, R.; Khan, M.; Tripathy, N.; Khan, M. I. R.; Khosla, A. Hydrothermally Synthesized Nickel Oxide Nanosheets for Non-Enzymatic Electrochemical Glucose Detection. *J. Electrochem. Soc.* **2020**, *167* (10), 107504. https://doi.org/10.1149/1945-7111/ab9757.

(76) Liu, M.; An, M.; Xu, J.; Liu, T.; Wang, L.; Liu, Y.; Zhang, J. Three-Dimensional Carbon Foam Supported NiO Nanosheets as Nonenzymatic Electrochemical H2O2 Sensors. *Appl. Surf. Sci.* **2021**, *542*, 148699. https://doi.org/10.1016/j.apsusc.2020.148699.

(77) Sivakumar, M.; Veeramani, V.; Chen, S.-M.; Madhu, R.; Liu, S.-B. Porous Carbon-NiO Nanocomposites for Amperometric Detection of Hydrazine and Hydrogen Peroxide. *Microchim. Acta* **2019**, *186* (2), 59. https://doi.org/10.1007/s00604-018-3145-3.

(78) Ramachandran, R.; Zhao, C.; Rajkumar, M.; Rajavel, K.; Zhu, P.; Xuan, W.; Xu, Z.-X.; Wang, F. Porous Nickel Oxide Microsphere and Ti3C2Tx Hybrid Derived from Metal-Organic Framework for Battery-Type Supercapacitor Electrode and Nonenzymatic H2O2 Sensor. *Electrochim. Acta* **2019**, *322*, 134771. https://doi.org/10.1016/j.electacta.2019.134771.

(79) Yu, Z.; Li, H.; Zhang, X.; Liu, N.; Zhang, X. NiO/Graphene Nanocomposite for Determination of H2O2 with a Low Detection Limit. *Talanta* **2015**, *144*, 1–5. https://doi.org/10.1016/j.talanta.2015.05.070.

(80) Liu, W.; Zhang, H.; Yang, B.; Li, Z.; Lei, L.; Zhang, X. A Nonenzymatic Hydrogen Peroxide Sensor Based on Vertical NiO Nanosheets Supported on the Graphite Sheet. *J. Electroanal. Chem.* **2015**, *749*, 62–67. https://doi.org/10.1016/j.jelechem.2015.04.037.

(81) Jana, S.; Samai, S.; Mitra, B. C.; Bera, P.; Mondal, A. Nickel Oxide Thin Film from Electrodeposited Nickel Sulfide Thin Film: Peroxide Sensing and Photo-Decomposition of Phenol. *Dalt. Trans.* **2014**, *43* (34), 13096–13104. https://doi.org/10.1039/C4DT01658K.

Figures

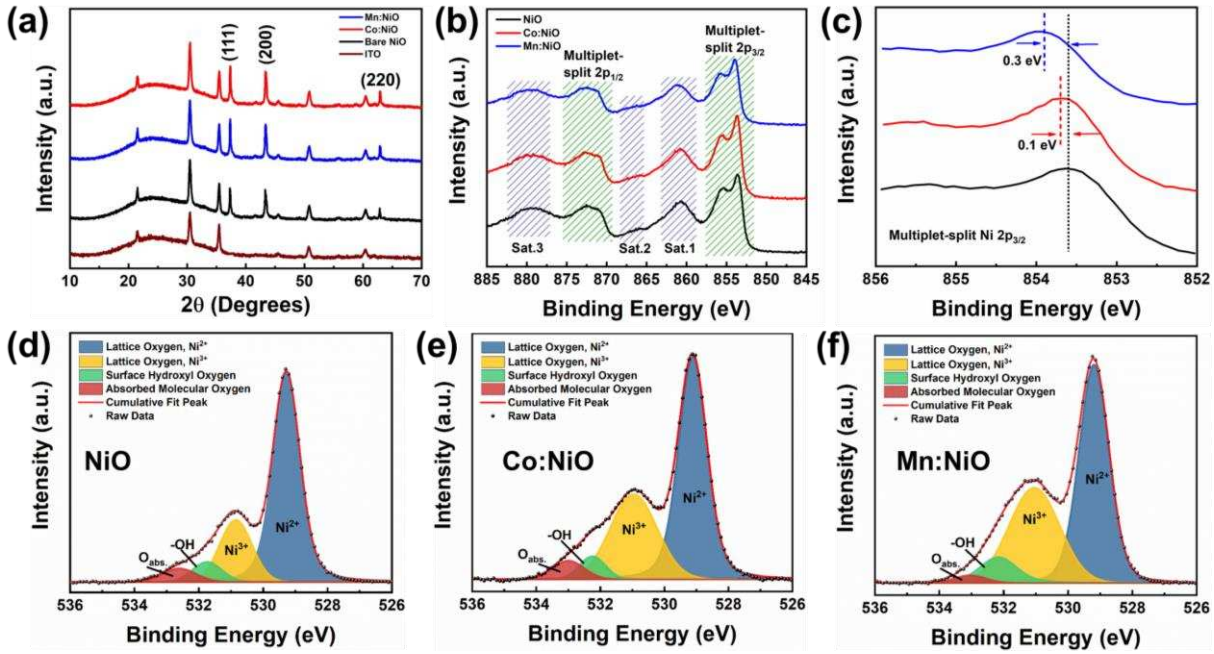

Fig. 1. (a) XRD patterns of ITO, NiO, Co:NiO and Mn:NiO thin films, (b) XPS spectra of Ni 2p, (c) enlarged spectra of Ni $2p_{3/2}$ and deconvoluted high-resolution XPS spectra of O 1s for (d) NiO, (e) Co:NiO, and (f) Mn:NiO thin films.

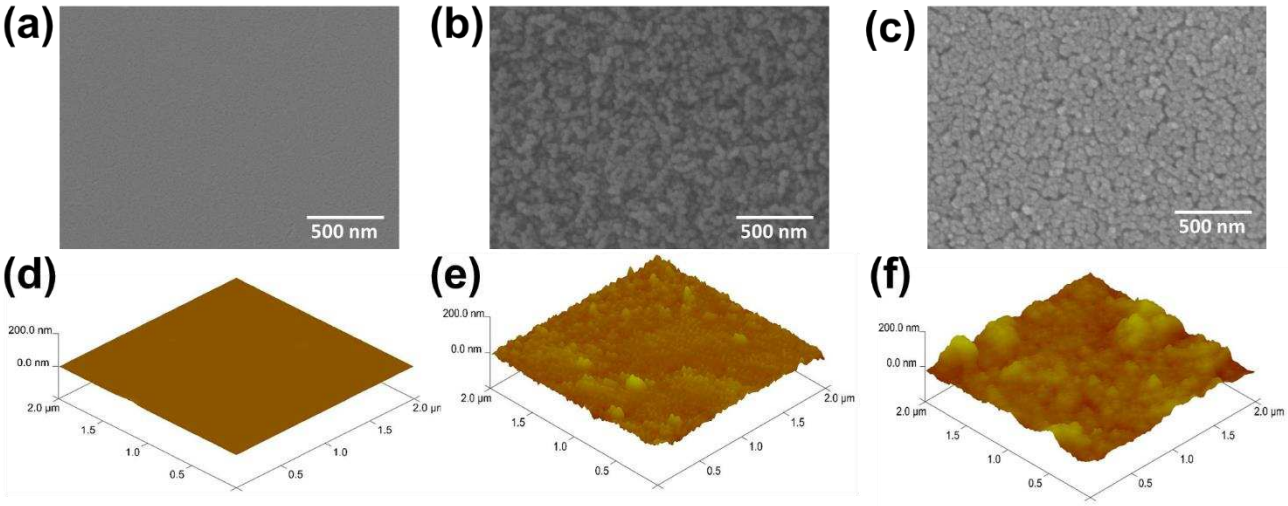

Fig. 2. SEM images of deposited (a) NiO, (b) Co:NiO, and (c) Mn:NiO thin films and the 3D AFM maps for (d) NiO, (e) Co:NiO, and (f) Mn:NiO thin films.

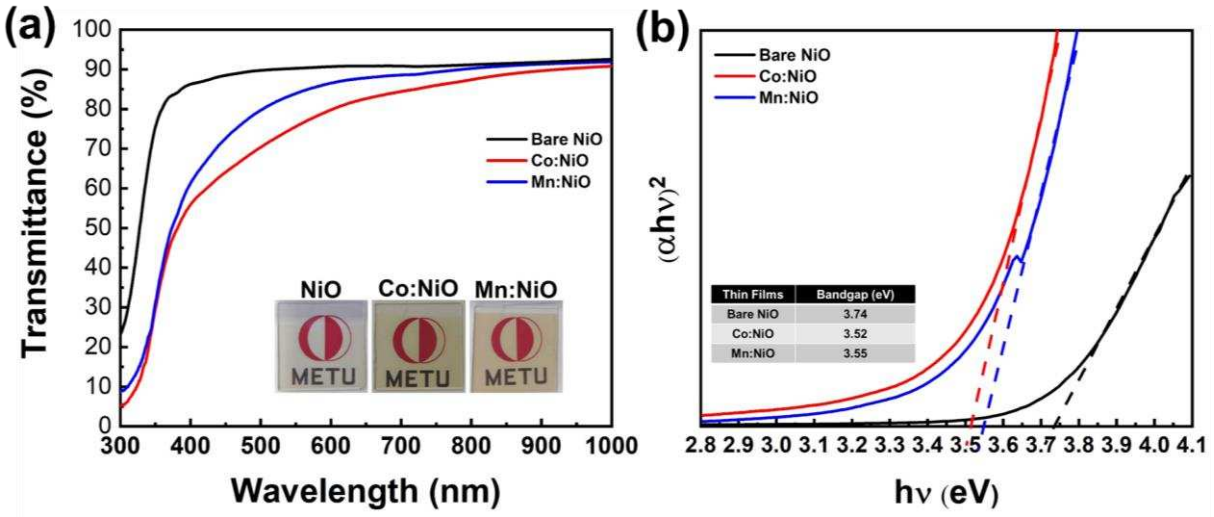

Fig. 3. (a) Transmittance spectra for bare NiO and M:NiO (Mn, Co) thin films. (Inset shows the photos of thin films on METU logo). (b) Tauc plots obtained from UV-VIS measurements for NiO and M:NiO (Mn, Co) thin films (Inset shows the bandgap values of thin films).

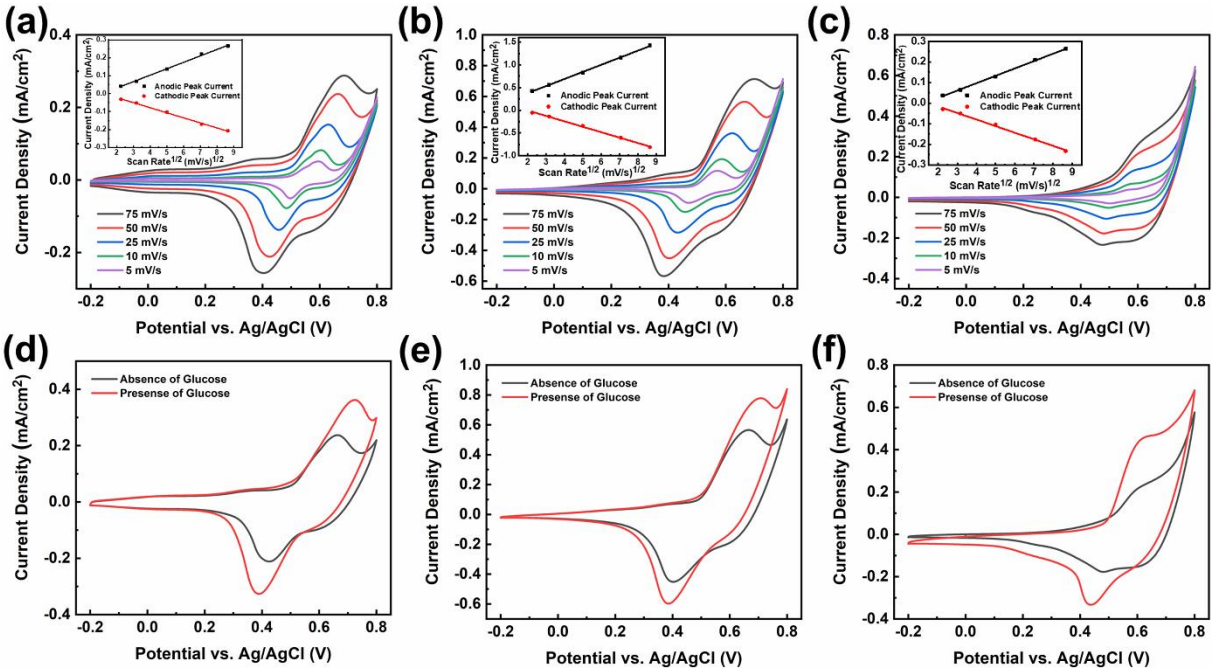

Fig. 4. CVs of (a) NiO, (b) Co:NiO, and (c) Mn:NiO thin films with different scan rates in 0.1 M NaOH (Insets show linear fittings of the anodic and cathodic peak currents *vs.* square root of scan rates). CV comparison of (d) NiO, (e) Co:NiO, and (f) Mn:NiO thin films in the absence and presence of glucose at a scan rate of 50 mV/s.

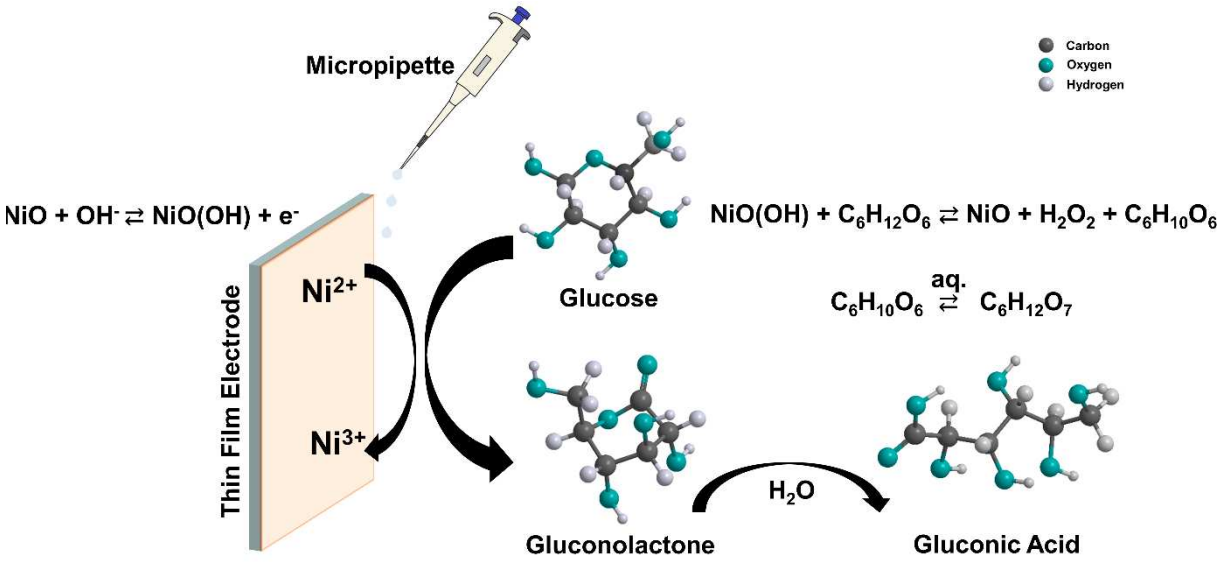

Fig. 5. Schematic illustration of the reactions occuring during amperometric glucose sensing.

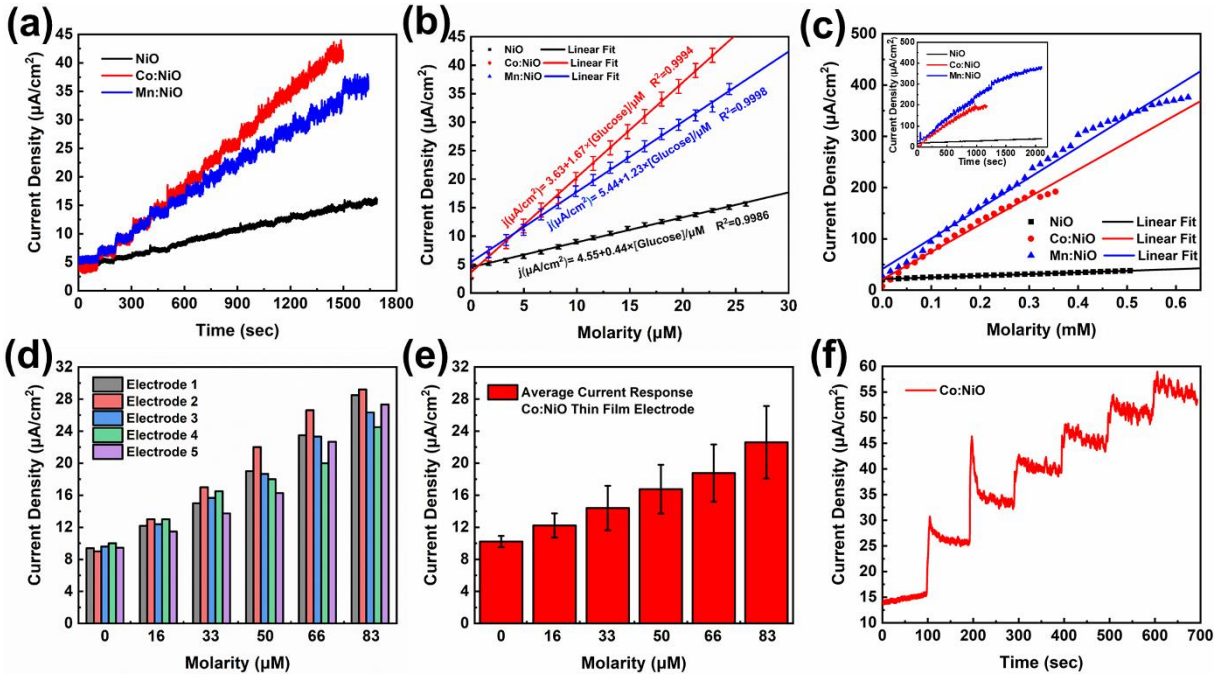

Fig. 6. (a) Amperometric current response of NiO, Co:NiO, and Mn:NiO thin film electrodes upon successive 1 mM glucose additions, (b) their linear calibration plots for current response *vs.* glucose concentration, (c) Calibration plots of NiO, Co:NiO, and Mn:NiO thin film electrodes upon successive 10 mM glucose addition (inset shows amperometric current response). (d) Amperometric current response of 5 different Co:NiO thin film electrodes upon successive 1 mM glucose addition. (e) 5 amperometric current response measurements on a Co:NiO thin film electrode upon successive 1 mM glucose addition and (f) amperometric response of Co:NiO thin film electrode upon addition of human serum. (0.65 V vs. Ag/AgCl was applied in all measurements.)

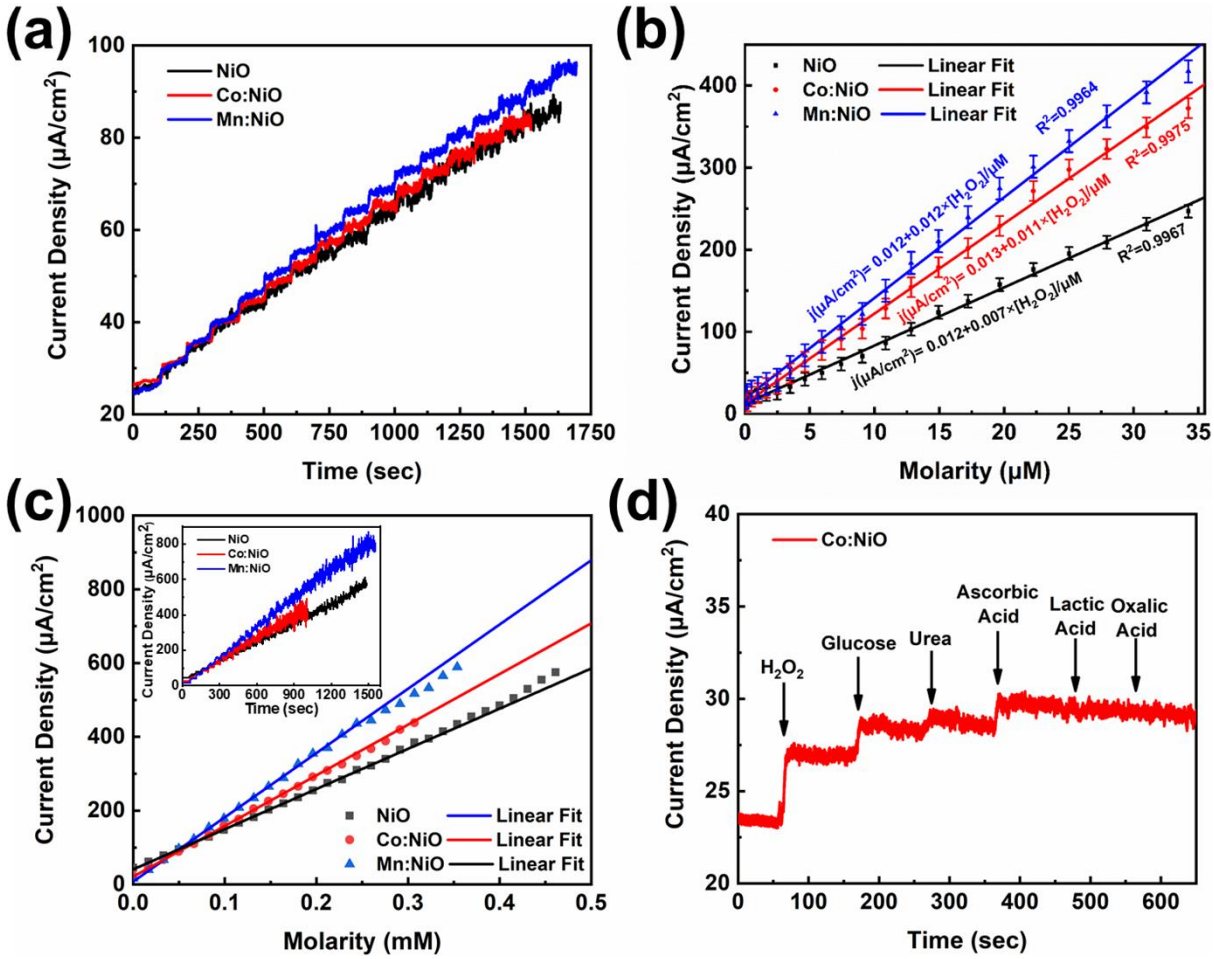

Fig. 7. (a) Amperometric current response of NiO, Co:NiO, and Mn:NiO thin film electrodes upon successive 1 mM H_2O_2 additions, (b) their linear calibration plots for current response *vs.* H_2O_2 concentration. (c) Calibration plots of NiO, Co:NiO, and Mn:NiO thin film electrodes upon successive 10 mM H_2O_2 addition (inset shows amperometric current response) and (d) amperometric current response of Co:NiO thin film electrodes upon addition of different analytes. (0.65 V vs. Ag/AgCl was applied in all measurements.)

Tables

Table 1. Performance comparison of amperometric glucose biosensors. (- means data is not provided).

Electrode	Sensitivity ($\mu A/\mu M \cdot cm^{-2}$)	LOD (nM)	Response Time (s)	Linear Range (µM)
NiO thin film*	**0.44**	**623**	**8.3**	**16-507**
Co:NiO thin film*	**1.67**	**231**	**5.4**	**16-308**
Mn:NiO thin film*	**1.23**	**404**	**6.4**	**16-293**
NiO HM/GCE [70]	**2.39**	**530**	**3**	**1.67-6870**
NiO/MWCNTs [71]	**1.77**	**2000**	**<5**	**10-7000**
NiO/NCS/GCE [72]	**0.40**	**250**	**-**	**1-800**
NiO NPs-NSs/GCE [73]	**1.14**	**180**	**-**	**1-400**
NiO-TiO_2/GCE [74]	**0.025**	**700**	**-**	**2-2000**
NiO nanosheets/gold [75]	**1.62**	**2500**	**-**	**250-3750**
NiO/SCCNTs [40]	**1.25**	**100**	**<2**	**2-2200**
NiO-Au NBs/GCE [35]	**0.05**	**1320**	**-**	**0-4550**
Mn:NiO/GCE [36]	**3.21**	**800**	**<5**	**2-670**
Porous NiO thin film [39]	**1.68**	**340**	**<4**	**0-1000**
NiO thin film [38]	**0.10**	**1050**	**5**	**1380-16660**

*This work.

Table 2. Performance comparison of amperometric H_2O_2 biosensors. (- means data is not provided).

Electrode	Sensitivity ($\mu A/\mu M \cdot cm^{-2}$)	LOD (nM)	Response Time (s)	Linear Range (µM)
NiO thin film*	**0.007**	**635**	**4.7**	**16-415**
Co:NiO thin film*	**0.011**	**558**	**2.9**	**16-307**
Mn:NiO thin film*	**0.012**	**664**	**2.4**	**16-276**
NiO Nanosheets on 3D Carbon Foam [76]	**0.023**	**13**	**-**	**200-3750**
Porous Carbon-NiO [77]	**0.107**	**1.5**	**-**	**0.01-3.9**
NiO [78]	**-**	**5400**	**-**	**10-570**
NiO/Graphene [79]	**0.591**	**766**	**~5**	**250-4750**
NiO Nanosheet on Graphite [80]	**1.077**	**400**	**-**	**Upto 4000**
NiO thin film [81]	**2.3**	**1280000**	**10**	**10-1000**

*This work.

Graphical Abstract